Copyright © 2007 American Scientific Publishers
All rights reserved
Printed in the United States of America

Journal of
Nanoscience and Nanotechnology
Vol. 8, 1–17, 2007

An Atomistically Enriched Continuum Model for Nanoscale Contact Mechanics and Its Application to Contact Scaling

Roger A. Sauer[1,*] and Shaofan Li[2]

Department of Civil and Environmental Engineering, University of California, Berkeley, CA 94720, USA

This work provides a comprehensive exposition and extension of an atomistically enriched contact mechanics model initially proposed by the present authors.[1] The contact model is based on the coarse-graining of the interaction occurring between the molecules of the contacting bodies. As these bodies may be highly compliant, a geometrically nonlinear kinematical description is chosen. Thus a large deformation continuum contact formulation is obtained which reflects the attractive and repulsive character of intermolecular interactions. Further emphasis is placed on the efficiency of the proposed atomistic-continuum contact model in numerical simulations. Therefore three contact formulations are discussed and validated by lattice statics computations. Demonstrated by a simple benchmark problem the scaling of the proposed contact model is investigated and some of the important scaling laws are obtained. In particular, the length scaling, or size effect, of the contact model is studied. Due to its formal generality and its numerical efficiency over a wide range of length scales, the proposed contact formulation can be applied to a variety of multiscale contact phenomena. This is illustrated by several numerical examples.

Keywords: Coarse-Graining, Continuum Contact Mechanics, Intermolecular Interaction, Nano-Mechanics, Scaling.

RESEARCH ARTICLE

1. INTRODUCTION

Due to the emergence of nano-science and nano-technology, contact mechanics and the understanding of contact/interaction phenomena at small scales are becoming increasingly important. Some of the examples governed by nanoscale interactions are atomic force microscopy,[2,3] nanoindentation,[4] nanotribology,[5] carbon nanotubes,[6–8] head-disk instabilities,[9] the adhesion of living cells[10] and the adhesion used by the Gecko.[11–13]

At the nanoscale level, the interaction of two or more bodies is governed by the interaction of individual atoms or molecules and can therefore be simulated by first-principle methods such as molecular dynamics. Examples of such computations include the study of carbon nanotubes,[14] proteins[15] and nanoindentation.[16] However, as illustrated by the Gecko example, problems governed by nanoscale interactions can still be macroscale in proportion. Since molecular dynamics traces the paths of all participating molecules, the method becomes prohibitively expensive and thus inefficient for such multiscale problems, both in terms of computational time and post-procession. A further disadvantage of molecular dynamics is that it does not blend into a continuum mechanical formulation, which is more suitable for problems at increasing length scales. To counter these deficiencies of molecular dynamics, several coarsened or homogenized descriptions have been proposed, like, for example, the 'quasi-continuum method,'[17,18] or the 'coarse-grained molecular dynamics' model.[19,20] The strength of both these multiscale methods is not only the reduction of computational cost compared to molecular simulations, but also the ability to couple regions of atomic resolution with regions of coarsened resolution. Initially, the methods have been developed to coarsen the internal behavior of a single body and have been successfully applied to various nanoscale problems. Recently, multiscale methods, like the quasi-continuum method, have also been used to study the contact interaction of multiple bodies.[21–24] In those works the interface between the contacting bodies is modelled up to the full atomic resolution, while a much coarser resolution is employed farther away from the region of contact. Even though a substantial increase in efficiency, compared to a full atomic resolution, is achieved, we feel that for

*Author to whom correspondence should be addressed.

some problems it becomes essential to also coarsen the region in contact, that is, to develop a computationally efficient contact formulation based on the homogenization of the interaction between individual molecules. This becomes particularly important when the length scale of a problem increases or when phenomena governed by long-range interaction, such as adhesion, are considered.

Efficient contact models describing the interaction between macroscale continua have been extensively investigated by the field of computational contact mechanics, e.g.,[25, 26] which has applications in a host of engineering fields, such as tribology, metal forming, manufacturing and structural failure analysis. However, current computational contact models are either formulated for macroscale problems, and thus are incapable of describing nanoscale interactions, like adhesion, or they only consider simplified interactions, e.g., by treating one of the bodies as rigid.[27, 28] Another common simplification is to consider infinitesimal deformations.[29] While such an assumption can be useful for the description of stiff solids, it becomes inadequate for strongly deforming materials and structures, such as are found in many bio-mechanical applications, like the Gecko adhesion.

In view of these limitations of present nanoscale and macroscale computational contact models, we seek a homogenized, large deformation continuum contact model based on nanoscale physics that can capture the coupling of two interacting bodies. The model should apply to a wide range of length scales and resort to a traditional continuum contact formulation at the macroscale. Therefore the computational formulation must be such that efficiency is maintained for increasing length scales without sacrificing accuracy. Such a continuum contact model, termed the 'Coarse Grained Contact Model' (CGCM) since it can be derived from the coarse-graining of molecular interactions, has been proposed by the present authors.[1] In that work the emphasis is placed on the computational formulation and its efficient implementation within a nonlinear finite element setting. In Ref. [30] we have further applied the model to dry adhesive contact and demonstrated its validity by a comparison with the analytical JKR,[31] DMT[32] and Maugis-Dugdale[33] models. In the present work, several further aspects of the CGC model are illustrated and investigated: A direct comparison of the CGCM with molecular statics is shown, to demonstrate the accuracy and efficiency of the proposed contact model. Secondly, by considering a simple benchmark problem the scaling of the CGC model is studied over a wide range of model parameters. Two scaling laws of the CGCM are obtained which characterize different aspects of the model behavior. This scaling discussion extends the preliminary results reported in Ref. [1]. Thirdly, we illustrate the application of the CGC model to the interaction of surface asperities as occurs during the sliding of two macroscale solids. Through such examples, macroscopic friction can be modelled based on a frictionless formulation on the microscale.

The following section outlines the proposed contact model, the Coarse Grained Contact Model. Section 3 is devoted to the scaling of the CGC Model. The application of the proposed model is further illustrated with the sliding example presented in Section 4. Conclusions are drawn in Section 5.

2. A CONTINUUM THEORY FOR NANOSCALE CONTACT

This section serves to outline the Coarse-Grained Contact Model (CGCM). We discuss the general idea and derive its governing equations. Its efficiency is illustrated and a simple comparison with a molecular simulation is shown.

2.1. General Idea

The objective of the Coarse-Grained Contact Model is to describe the interaction, like adhesion and contact, between deforming, nanoscale bodies. The model can be related to classical molecular dynamics and continuum contact mechanics as is illustrated in Figure 1. In the following, these three models and the two procedures, which facilitate a transition between the models, are discussed. The formulas appearing in Figure 1 are subject of Section 2.2.

Molecular dynamics[34] is a discrete model which describes the interaction of an assembly of point masses, usually molecules or atoms. The particle interaction is modelled by intermolecular interaction potentials, e.g., see Ref. [35]. An example is the Lennard-Jones potential modelling pairwise interaction. By choice, we group the interaction potentials into two categories: *intrasolid* and *intersolid* potentials. The first group denotes the interaction of particles within the bodies (potentials ψ_1 and ψ_2 in Figure 1). The second category denotes the interactions of particles belonging to distinct bodies (potential ϕ in Figure 1). The motivation behind this distinction is that the intersolid potential ϕ is often weak but long-range, like for example van der Waals interaction, while the intrasolid potential ψ is often strong but short-range, like covalent, ionic or metallic bonds. The nomenclature is in analogy to the description of interlayer and intralayer carbon nanotube interactions.[8] Molecular simulations become less useful for increasing length and time scales due to the computational cost associated with many degrees of freedom.

Continuum mechanics[36, 37] on the other hand offers a formulation which is well established for macroscale problems and which can be efficiently implemented in numerical computations, for example in the finite element method.[38–40] The drawback of applying classical continuum approaches to nanoscale problems is that these approaches are typically based on phenomenological models and lack the atomistic information.

The basic idea of the CGC Model is to combine the physics of atomic interaction during contact with the

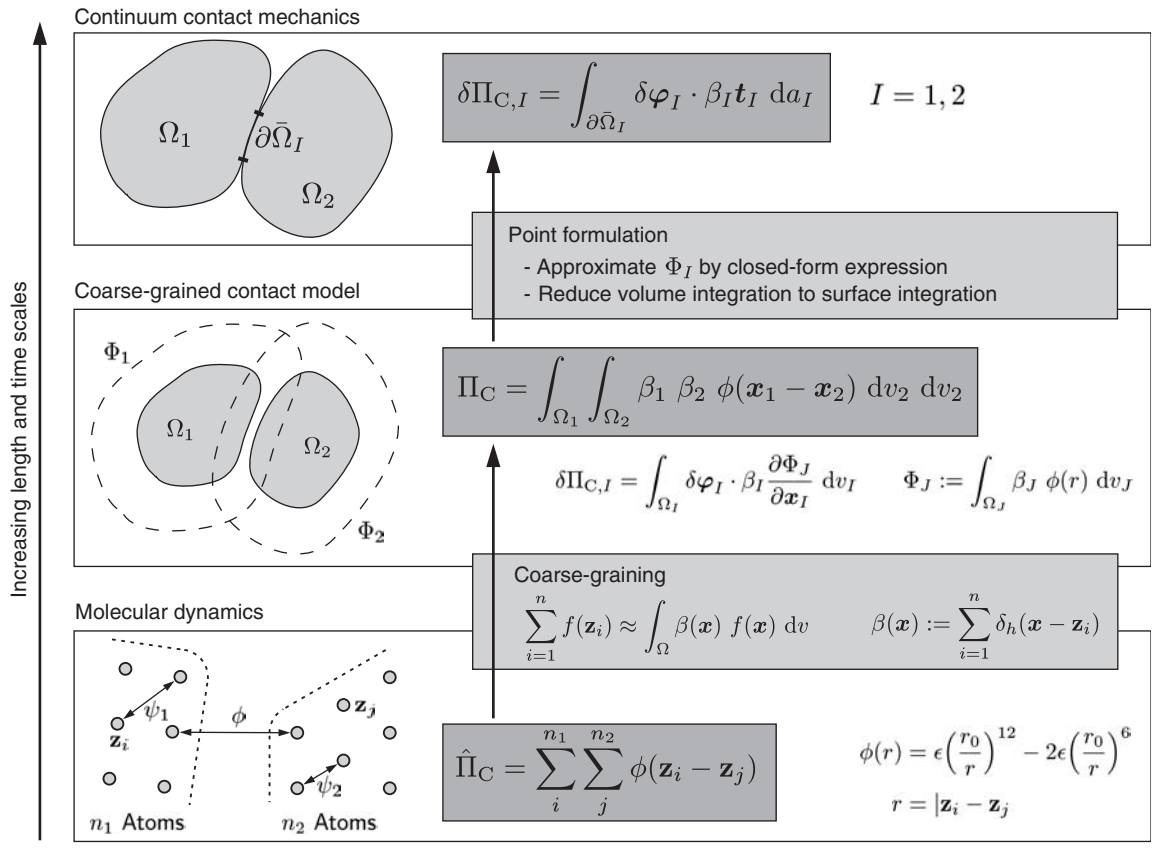

Fig. 1. Relation of the Coarse-Grained Contact Model (CGCM) with classical molecular dynamics and continuum contact mechanics.

elegance and numerical applicability of a continuum formulation. This is achieved by the coarse-graining, or homogenization, of the molecular dynamics model, as indicated in Figure 1. Thus, the coarse-graining procedure is a transitional scheme which is used to construct an effective continuum model, the CGC model, from molecular dynamics. The coarse-graining procedure is two-fold: The intrasolid interaction is homogenized into a continuum constitutive model, like e.g., the Cauchy-Born rule,[41] while the intersolid interaction is homogenized into a continuum interaction energy, which describes phenomena like adhesion and contact. As the former contribution has been studied before, e.g.,[18] and references therein, the focus of this work is placed on the second part, i.e., the study of the homogenized continuum interaction energy, which is denoted by Π_C in Figure 1. By the homogenization of the intersolid potential ϕ, a continuous field Φ_I, surrounding each body Ω_I, is obtained. As a second body enters field Φ_I, it experiences a force field, which captures the interaction of the two bodies. The coarse-graining procedure and the equations contained in Figure 1 are discussed in detail in the following section. Within this work we consider only spatial coarse-graining. To dampen high frequency oscillation a temporal coarse-graining scheme should be considered.[19, 20] Remarks on the extension of the CGCM to temporal coarse-graining are discussed in Ref. [42].

As is shown by the example following in Section 2.4, a straightforward numerical formulation of the CGC model can become inefficient, especially as the length scale of the problem increases. It therefore becomes vital to introduce appropriate approximations in the formulation of the CGCM, such that efficiency is restored while maintaining accuracy. An example of such an efficient approximation is the 'point formulation' discussed in Section 2.3 and outlined in Figure 2. Formally, this approximation can be classified as a traditional computational continuum contact model—one, which is based on the underlying atomistic physics. The 'point formulation' therefore facilitates the transition between the two models, as is shown in Figure 1. Due to this transition the CGC model constitutes an efficient model, which is capable of describing contact at a wide range of length scales, ranging from the atomic scale of nanometers to the macroscopic scale of millimeters.

The CGC model is motivated as a homogenized, effective treatment for contact/interaction problems at very small scales. It is cast into an efficient, computational continuum contact formulation, which accounts for large deformations and can thus describe the strong nonlinear coupling of strongly deforming, soft bodies. It is important to note that the CGC model cannot capture the atomic details, as they are deliberately coarsened in the construction of the model. Therefore, phenomena like dislocation

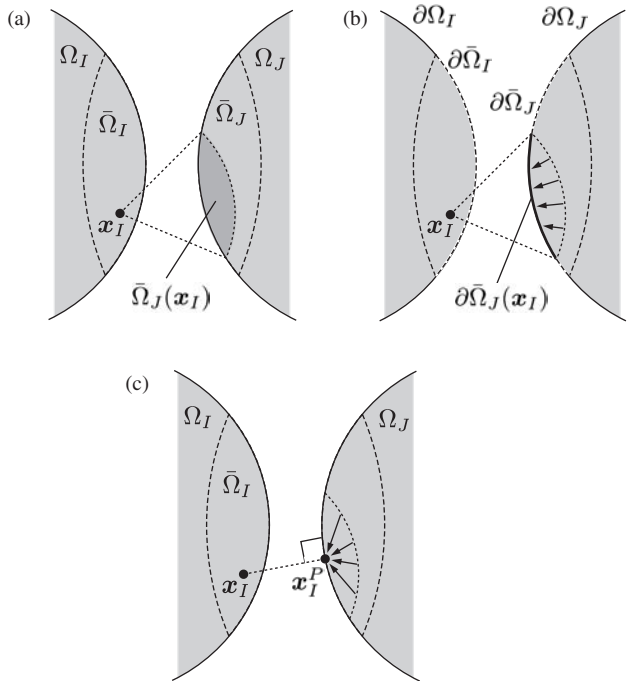

Fig. 2. Types of interaction: (a) Volume interaction (VI); (b) Surface interaction (SI); (c) Point interaction (PI).

motion, fracture, atomic vibrations, surface relaxation or chemical reactions cannot be described at the atomic level by the present model. In principle, this can be achieved by coupling the CGC model with an atomistic model such as molecular dynamics.

2.2. Governing Equations

With the proposed nanoscale contact model introduced, we proceed in deriving its governing equations. We start by considering the interaction of two distinct bodies occupying the current configurations Ω_1 and Ω_2 and containing n_1 and n_2 atoms. The total potential energy of the two body system can be written as (Ref. [1])

$$\Pi = \sum_{I=1}^{2} \big[\Pi_{\text{int},I} - \Pi_{\text{ext},I}\big] + \Pi_{\text{C}} \tag{1}$$

where $\Pi_{\text{int},I}$ and $\Pi_{\text{ext},I}$ are the internal and external energies of body Ω_I ($I = 1, 2$), and where Π_{C} denotes the contact interaction energy between bodies Ω_1 and Ω_2. (Throughout this paper we use upper case indices to denote the bodies and lower case indices to denote the particles constituting the bodies.) The contributions $\Pi_{\text{int},I}$, $\Pi_{\text{ext},I}$ and Π_{C} are formulated for a discrete molecular system and then coarse-grained into an effective continuum description (this transition is also indicated Figure 1). For this, consider a body Ω containing n atoms with position $\mathbf{z}_i$, $i \in \mathcal{I}$, where $\mathcal{I}$ is the set of all n indices i. Suppose $f(\mathbf{z}_i)$ is a smooth function defined on Ω. To coarse-grain the discrete system we consider the following approximation

$$\sum_{i\in\mathcal{I}} f(\mathbf{z}_i) \approx \int_\Omega \beta(\boldsymbol{x}) f(\boldsymbol{x})\, dv_{\boldsymbol{x}} \tag{2}$$

that is, we replace the discrete sum of $f(\mathbf{z}_i)$ over all atomic sites $\mathbf{z}_i$ by the continuous integral over $\boldsymbol{x} \in \Omega$. In Eq. (2) β is the atomic density of the continuum, written as

$$\beta(\boldsymbol{x}) := \sum_{i\in\mathcal{I}} \delta_h(\boldsymbol{x} - \mathbf{z}_i) \tag{3}$$

and constructed from the Gaussian distribution in $\mathbb{R}^d$

$$\delta_h(\mathbf{y}) := \frac{1}{(\sqrt{\pi}h)^d} \exp\Big(-\frac{\mathbf{y}\cdot\mathbf{y}}{h^2}\Big) \tag{4}$$

The atomic density β is measured in *number of particles per current volume*. Operation (2) is exact if $h \to 0$, i.e., δ_h approaches the Dirac delta function δ. Equation (2) is also exact, for all h, if $f(\boldsymbol{x})$ is a linear function of $\boldsymbol{x}$. Very good accuracy is thus achieved if h is such that $f(\boldsymbol{x})$ is approximately linear within the support space of δ_h. Furthermore, if the particles are arranged in a regular lattice and if h is larger that the lattice spacing, then β can be treated as constant across the domain.

To illustrate the accuracy of operation (2) let us examine the one-dimensional coarse-graining in infinite space. A given function $f(x)$ is thus approximated by

$$g(x) = \int_{-\infty}^{\infty} \delta_h(x - y) f(y)\, dy \tag{5}$$

As an example, consider the family of waves $f_\lambda(x) = \cos(2\pi x/\lambda)$ characterized by the wavelength λ. For this function, integral (5) can be evaluated exactly. We find $g_\lambda(x) = \exp(-\pi^2 h^2/\lambda^2)\, f_\lambda(x)$ so that the error of this approximation, in dependence of coarse-graining parameter h and wavelength λ, is

$$e(h,\lambda) := \frac{f_\lambda(x) - g_\lambda(x)}{f_\lambda(x)} = 1 - \exp\Big(-\frac{\pi^2 h^2}{\lambda^2}\Big) \tag{6}$$

As the parameter $h \to 0$ or as the wavelength $\lambda \to \infty$, the error vanishes ($e \to 0$); on the other hand as $h \to \infty$ or $\lambda \to 0$, we approach 100% error ($e \to 1$), i.e., all information of f_λ is lost in g_λ. To capture a given oscillation f_λ, with given λ, up to a maximum error of 5% the coarse-graining parameter h must satisfy $h < 0.0721\lambda$. Conversely, a given coarse-graining scheme, with given h, can only capture oscillations with wavelengths above $\lambda \approx 13.87h$. Thus h can be viewed as a parameter regulating what kind of fine scale information is captured accurately up to a certain tolerance and what kind is lost entirely.

The coarse-graining of the particle description into an effective continuum has a similar effect than the coarsening caused by a numerical discretization, e.g., with finite

RESEARCH ARTICLE

elements. To capture the oscillation f_λ with equidistant linear finite elements, up to an error of 5% in the L_2 norm, around nine elements, with lengths $\ell_e = \lambda/9$, are needed. A finite element approximation thus corresponds to a coarse-graining where h is of the order of the element length ℓ_e.

The coarse-graining operation, defined by Eqs. (2)–(4), is a simple transitional procedure illustrating how an effective continuum formulation can be derived from a particle description. The procedure is a reminiscence of the derivation of 'Smoothed Particle Hydrodynamics'[43, 44]—a meshfree particle method developed for computational astrophysics, fluid dynamics and solid mechanics. Other coarse-graining approaches can be found in the works of Refs. [45] and [20].

In the following discussion we consider only pairwise interaction of particles. Such interactions are described by two-point interaction potentials, denoted by ϕ and ψ_I in Figure 1 (where either $I = 1$ or $I = 2$). As mentioned before we distinguish between the interaction of particles within one body Ω_I and the interaction of particles belonging to two distinct bodies Ω_1 and Ω_2. The former is termed the *intrasolid* interaction and is denoted by ψ_I; the latter is termed the *intersolid* interaction and is denoted by ϕ. Considering only pairwise interaction, the internal energy of the discrete n_I particle system is given by the double summation over all atoms $\mathbf{z}_i$ within Ω_I

$$\widehat{\Pi}_{\text{int},I} = \sum_{i\in\mathcal{J}_I} \Psi_I(z_i), \quad \Psi_I(z_i) := \frac{1}{2}\sum_{k\in\mathcal{J}_I}^{k\neq i} \psi_I(r_{ik})$$
$$r_{ik} = |z_i - z_k|, \quad I = 1, 2 \tag{7}$$

The factor $1/2$ is needed since every atomic bond, described by the interaction potential ψ_I, is counted twice in the double summation above. According to expression (2) the internal energy (7) is coarse-grained as

$$\widehat{\Pi}_{\text{int},I} \approx \Pi_{\text{int},I} = \int_{\Omega_I} \beta_I(\boldsymbol{x})\Psi_I(\boldsymbol{x})\, dv_I \tag{8}$$

where

$$\Psi_I(\boldsymbol{x}) = \frac{1}{2}\sum_{k\in\mathcal{J}_I} \psi_I(r_k), \quad r_k = |\boldsymbol{x} - \mathbf{z}_k|, \quad \mathbf{z}_k \neq \boldsymbol{x} \tag{9}$$

To distinguish between the discrete and continuum internal energies of Eqs. (7) and (8), a hat is used for the former case. The integrand $w_I := \beta_I\Psi_I$ of Eq. (8) is the stored energy density (per current volume) within body Ω_I. The coarse-grained internal energy $\Pi_{\text{int},I}$ hence takes the same form usually considered in continuum mechanics, e.g., see Ref. [36].

2.2.1. Remarks

(1) Equation (9) expresses the total energy $\Psi(\boldsymbol{x})$ at site $\boldsymbol{x}$ due to the interaction with all neighboring particles $\mathbf{z}_k$. In practice only a close shell of surrounding particles is included in the sum, since the potential ψ decays with distance r_k. An efficient method to evaluate Eq. (9), valid under certain assumptions on the deformation at $\boldsymbol{x}$, is the Cauchy-Born rule, see Refs. [41], [46], and also [17].
(2) The formulation of the internal energy in Eqs. (7)–(9) can be extended beyond pair potentials, e.g., to three-point potentials, or to embedded atom (EAM) type potentials.[47]
(3) The site energy $\Psi(\boldsymbol{x})$ (9) is fundamentally different for bulk atoms, which are fully surrounded by neighboring atoms, than for surface atoms, which are only partly surrounded by neighboring atoms. This gives rise to a surface energy, which leads to important phenomena such as the surface tension of fluids or surface relaxation effects of solids. The coarse-graining formalism presented above can be extended to include such surface effects, however, this is not considered here. An approach to formalize the surface energy within the Cauchy-Born formalism is discussed in Ref. [48].

Next, we consider the interaction energy between two bodies Ω_1 and Ω_2. Let $\mathbf{z}_i$, $i \in \mathcal{J}_1$, denote the position of the n_1 particles within Ω_1 and $\mathbf{z}_j$, $j \in \mathcal{J}_2$, denote the position of the n_2 particles of Ω_2. If pairwise interaction is considered the interaction energy of the discrete system is given by

$$\widehat{\Pi}_C = \sum_{i\in\mathcal{J}_1}\sum_{j\in;_2} \phi(r_{ij}), \quad r_{ij} = |\mathbf{z}_i - \mathbf{z}_j| \tag{10}$$

where $\phi(r)$ is the intersolid interaction potential between the two particles at $\mathbf{z}_i$, $i \in \mathcal{J}_1$, and $\mathbf{z}_j$, $j \in \mathcal{J}_2$. An example for the intersolid interaction is the van der Waals attraction between particles. Compared to covalent, ionic and metallic bonds, van der Waals interaction is weaker but acts over larger distances. Van der Waals attraction is often modelled by the Lennard-Jones potential

$$\phi(r) = \epsilon_0\left(\frac{r_0}{r}\right)^{12} - 2\epsilon_0\left(\frac{r_0}{r}\right)^{6} \tag{11}$$

where the $1/r^{12}$ term is empirical and models the repulsion which occurs when the atoms are in close proximity. Here, the length $r = r_0$ is the equilibrium spacing between the particles where the force $F(r) := -\frac{\partial\phi}{\partial r}$ vanishes. The energy ϵ_0 corresponds to the energy required to separate the particles from $r = r_0$ to $r = \infty$. The Lennard-Jones potential (11) is a particular example for the intersolid potential ϕ, which we consider in the remainder of this paper. Applying the coarse-graining operation (2) to the double summation of expression (10) yields

$$\widehat{\Pi}_C \approx \Pi_C = \int_{\Omega_1}\int_{\Omega_2} \beta_1\beta_2\phi(r)\, \mathrm{d}v_2\mathrm{d}v_1, \quad r = |\boldsymbol{x}_1 - \boldsymbol{x}_2| \tag{12}$$

the homogenized interaction energy of the two continua. Here β_1 and β_2 denote the current particle density at points $\boldsymbol{x}_1 \in \Omega_1$ and $\boldsymbol{x}_2 \in \Omega_2$. For now we suppose that there is no flux of particles into or out of the bodies. Therefore the

RESEARCH ARTICLE

number of particles within a given volume is conserved during deformation, i.e.,

$$\beta_I \mathrm{d}v_I = \text{const.} \quad \text{for } I = 1, 2 \tag{13}$$

For the further developments it becomes advantageous to pull-back the integral over the current, deformed configurations Ω_1 and Ω_2, to the integral over the reference, usually undeformed, configurations Ω_{10} and Ω_{20}. According to Eq. (13), the pull-back of expression (12) becomes

$$\Pi_{\mathrm{C}} = \int_{\Omega_{10}} \int_{\Omega_{20}} \beta_{10}\beta_{20}\phi(r)\mathrm{d}V_2\mathrm{d}V_1 \tag{14}$$

Here β_{I0}, $I = 1, 2$, is the reference density measured in *number of particles per reference volume*, and $\mathrm{d}V_I$ is a referential volume element. Consider the two motions φ_1 and φ_2 mapping the reference points $X_1 \in \Omega_{10}$ and $X_2 \in \Omega_{20}$ onto the current locations $x_1 \in \Omega_1$ and $x_2 \in \Omega_2$. Associated with the two motions are the two deformation gradients $F_1 = \mathrm{Grad}\varphi_1$ and $F_2 = \mathrm{Grad}\varphi_2$, where the gradient operator $\mathrm{Grad}(\ldots)$ is taken with respect to the reference configurations Ω_{10} and Ω_{20}. Given the Jacobian determinant $J_I = \det F_I$, $I = 1, 2$, of the deformation, the spatial quantities β_I and $\mathrm{d}v_I$ can be related to the material quantities β_{I0} and $\mathrm{d}V_I$ by

$$\beta_I = \beta_{I0}/J_I, \quad \mathrm{d}v_I = J_I \mathrm{d}V_I \tag{15}$$

2.2.2. Remarks

(1) If Ω_1 and Ω_2 are of simple geometry and their deformation is neglected (or simplified), Π_{C} may be evaluated analytically.[49] This approach dates back to the 1930's with the seminal works of Bradley[50] and Hamaker.[51] Formulation (12) has also been considered in the computational study of carbon nanotubes.[52, 8]

(2) The framework of Eq. (12) can be easily extended to describe surface interaction, e.g., for coated, charged particles, and to describe multi-body interaction.[1]

(3) The present formulation of Π_{C} admits only pair potentials ϕ, like the Lennard-Jones potential. In principle also multi-point potentials, like three-point potentials, can be considered in the interaction energy Π_{C}.

With Eqs. (8) and (12) we have obtained a continuum formulation of the internal energy Π_{int} and the contact interaction energy Π_{C}. By further use of coarse-graining operation (2), one can also derive continuum expressions of the external energy Π_{ext} or the kinetic energy K, as is shown in Ref. [1]. Thus, a continuum contact model, the CGCM, is obtained by the coarse-graining of the underlying discrete particle description. This transition is also illustrated in Figure 1.

To implement the CGC model into a numerical approach, such as the finite element method, we need to obtain its governing weak form. We therefore need the variation of the total potential energy Π (1), which is expressed as

$$\delta\Pi = \sum_{I=1}^{2} \left[\delta\Pi_{\mathrm{int},I} + \delta\Pi_{\mathrm{C},I} - \delta\Pi_{\mathrm{ext},I}\right] \tag{16}$$

The variation of the internal energy, also denoted as the internal virtual work, can be written as

$$\delta\Pi_{\mathrm{int},I} = \int_{\Omega I} \mathrm{grad}(\delta\varphi_I) : \boldsymbol{\sigma}_I \, \mathrm{d}v_I \tag{17}$$

e.g., see.[38] Here $\boldsymbol{\sigma}_I$ is the Cauchy stress tensor of body Ω_I. It follows from the considered constitutive relation. An example is the Cauchy-Born rule based on expression (9).[1] One can also combine the CGC model with phenomenological constitutive approaches[53] as is considered in (Refs. [42] and [30]). Due to Eq. (13) the variation of the contact energy Π_{C} becomes

$$\delta\Pi_{\mathrm{C}} = \sum_{I=1}^{2} \delta\Pi_{\mathrm{C},I}$$

$$\delta\Pi_{\mathrm{C},I} = \int_{\Omega_1} \int_{\Omega_2} \beta_1\beta_2 \frac{\partial\phi(r)}{\partial \boldsymbol{x}_I} \cdot \delta\varphi_I \, \mathrm{d}v_2\mathrm{d}v_1 \tag{18}$$

Alternatively, contribution $\delta\Pi_{\mathrm{C},I}$ can also be written as

$$\delta\Pi_{\mathrm{C},I} = -\int_{\Omega_I} \delta\varphi_I \cdot \beta_I \mathbf{b}_I \, \mathrm{d}v_I \tag{19}$$

where $\mathbf{b}_I$ denotes a body force acting at $\boldsymbol{x}_I \in \Omega_I$ and given by

$$\mathbf{b}_I(\boldsymbol{x}_I) := -\frac{\partial\Phi_J}{\partial \boldsymbol{x}_I}, \quad \Phi_J := \int_{\Omega_J} \beta_J \phi(r) \, \mathrm{d}v_J \tag{20}$$

Here J is the subscript of the neighboring body. That is, we either have $I = 1$ and $J = 2$ or $I = 2$ and $J = 1$. As illustrated in Figure 1, Φ_J constitutes a field surrounding body Ω_J and which invokes the body forces $\mathbf{b}_I$ inside the neighboring body Ω_I. According to Eq. (19) the variation $\delta\Pi_{\mathrm{C},I}$ can be understood as the virtual work of the contact body forces $\mathbf{b}_I$. Defining the unit direction vector

$$\bar{\mathbf{r}}_I := \frac{\mathbf{r}_I}{r}, \quad \mathbf{r}_I := \boldsymbol{x}_I - \boldsymbol{x}_J, \quad r := |\mathbf{r}_I| \tag{21}$$

and using

$$\frac{\partial\phi(r)}{\partial \boldsymbol{x}_I} = \frac{\partial\phi}{\partial r}\frac{\partial r}{\partial \boldsymbol{x}_I} = -F(r)\bar{\mathbf{r}}_I \tag{22}$$

where $F(r) = -(\partial\phi/\partial r)$ is the force associated with $\phi(r)$, the body force $\mathbf{b}_I$ can also be written as

$$\mathbf{b}_I(\boldsymbol{x}_I) = \int_{\Omega_J} \beta_J \; F(r)\bar{\mathbf{r}}_I \, \mathrm{d}v_J \tag{23}$$

As is seen, the body force $\mathbf{b}_I$ depends explicitly on the density β_J, the distance vector $\mathbf{r}_I$, and the current configuration Ω_J of the neighboring body. This leads to a strong nonlinear coupling between bodies Ω_1 and Ω_2 during

interaction. In[1] it is shown, that for some restrictive, special cases, Eq. (23) can be evaluated analytically, simplifying the contact formulation considerably.

Given the variation (16) and contributions (17) and (18), the weak form, governing the proposed continuum interaction model, follows from the principle of stationary potential energy as

$$\sum_{I=1}^{2}\Big[\int_{\Omega_I} \mathrm{grad}(\delta\varphi_I) : \boldsymbol{\sigma}_I \, \mathrm{d}v_I - \int_{\Omega_I} \delta\varphi_I \cdot \beta_I \mathbf{b}_I \, \mathrm{d}v_I - \delta\Pi_{\mathrm{ext},I}\Big] = 0 \ , \quad \forall\ \delta\varphi_I \quad (24)$$

2.2.3. Remarks

(1) The weak form statement (24) can be extended by inertial contributions obtained from the kinetic energy of the two-body system, as is shown in.[1] This extension is not considered within this paper as we restrict ourselves to quasi-static examples.
(2) In principle, the interaction between the two bodies, as modelled by Eq. (11), extends to infinity. This implies that the undeformed configurations Ω_{10} and Ω_{20} are infinitely far apart. On the other hand, since ϕ usually decays, it is useful to neglect the interaction beyond a cutoff distance r_c, as is discussed in the following section.
(3) The reference density β_0 can be considered a constant across the domain Ω_0, if the particles are distributed evenly and if the coarse-graining parameter h exceeds the particle spacing. For this case, which is considered in the following examples, the actual value of h does not play a role anymore.

We emphasize that Eq. (24) is formulated in the nonlinear framework of continuum mechanics of large deformations[36,37] and that this weak form can be readily incorporated into a nonlinear finite element setting.[1] The essence of the CGC model is the description of small scale contact using the atomistically enriched continuum interaction energy Π_C (12) and its efficient numerical implementation. As illustrated in Figure 1 the coarse-graining procedure and the 'point formulation' establish the connections between a molecular description, the CGCM and a traditional continuum contact formulation.

2.3. Efficient Evaluation of the Virtual Contact Work $\delta\Pi_C$

In Ref. [1] we have derived and implemented three different finite element formulations, to evaluate the contact integral $\delta\Pi_C$ given in Eq. (18). These formulations are examples of the three general classes of interaction formulations, shown in Figure 2: The interaction of two bodies may be described as an interaction of (a) their volumes, (b) their surfaces or (c) individual points. According to this classification, the virtual contact work $\delta\Pi_C$ can be approximated by the following three methods.

Consider the force $\mathbf{b}_I$ (23) acting at point $x_I \in \Omega_I$ and invoked by the presence of neighboring body Ω_J. (In the case of two interacting bodies we either have $I = 1, J = 2$ or $I = 2, J = 1$.) If we consider a cutoff range, r_c, of the interaction potential ϕ, the influence at $\boldsymbol{x}_I$ is restricted to the subdomain $\bar{\Omega}_J(\boldsymbol{x}_I) \subset \Omega_J$, as is shown in Figure 2(a). The cutoff radius also implies that body forces $\mathbf{b}_I$ are only invoked within a certain region $\bar{\Omega}_I \subset \Omega_I$. From geometrical considerations follows that we have the ordering $\bar{\Omega}_J(\boldsymbol{x}_I) \subset \bar{\Omega}_J \subset \Omega_J$ and $\partial\bar{\Omega}_J(\boldsymbol{x}_I) \subset \partial\bar{\Omega}_J \subset \partial\Omega_J$ for both bodies ($J = 1, 2$). By introducing a cutoff radius the integration of Eqs. (19) and (23) can thus be reduced to

$$\begin{aligned} \delta\Pi_{C,I} &= -\int_{\bar{\Omega}_I} \delta\varphi_I \cdot \beta_I \mathbf{b}_I \mathrm{d}v_I, \\ \mathbf{b}_I(\boldsymbol{x}_I) &= \int_{\bar{\Omega}_J(\boldsymbol{x}_I)} \beta_J F(r) \bar{\mathbf{r}}_I \mathrm{d}v_J \end{aligned} \quad (25)$$

If the cutoff radius r_c is much smaller than the extent of the two bodies, formulation (25) furnishes a considerable reduction in the computational cost compared to the original formulation. On the other hand if $r_c \to \infty$ we have $\bar{\Omega}_I = \Omega_I$ and $\bar{\Omega}_J(\boldsymbol{x}_I) = \Omega_J$ so that the original formulation is recovered. Eq. (25) poses the basis for the first useful implementation of the CGC model. It is referred to as 'volume interaction formulation' (VI) and shown conceptually in Figure 2(a). Formulation (25) involves no approximation in the evaluation of $\delta\Pi_C$ other than the negligence of interactions beyond r_c.

The volume integration of formulation 'VI' can still become very costly, as is demonstrated by the comparison of Section 2.4. This motivates the following two efficient approximations, denoted as 'surface interaction' (SI) and 'point interaction' (PI) formulation and shown in Figures 2(b) and (c). The idea of formulation 'SI' is to map the region $\bar{\Omega}_J(\boldsymbol{x}_I)$ onto its outer boundary $\partial\bar{\Omega}_J(\boldsymbol{x}_I)$ and thus reduce the volume interaction to a surface interaction. Hence, expression $(25)_2$ is further simplified to

$$\mathbf{b}_I(\boldsymbol{x}_I) = \int_{\partial\bar{\Omega}_J(\boldsymbol{x}_I)} \beta_J \ \bar{F}(r) \ \bar{r}_I \ \mathrm{d}a_J \quad (26)$$

The bar on top of the force $\bar{F}(r)$ is used to indicate that the expression for the force changes from Eq. $(25)_2$ to Eq. (26), due to the mapping $\bar{\Omega}_J(\boldsymbol{x}_I) \to \partial\bar{\Omega}_J(\boldsymbol{x}_I)$. Formulation 'PI' further concentrates the region $\bar{\Omega}_J(\boldsymbol{x}_I)$ into a single point, the closest projection point $\boldsymbol{x}_I^P$ of $\boldsymbol{x}_I$. The body force at $\boldsymbol{x}_I$ is thus obtained by a single function evaluation, i.e.,

$$\mathbf{b}_I(\boldsymbol{x}_I) = \bar{\bar{F}}(r_I^P)\bar{r}_I^P \quad (27)$$

where $r_I^P := |r_I^P|, r_I^P := \boldsymbol{x}_I - \boldsymbol{x}_I^P$, is the distance between point x_I and surface $\partial\Omega_J$, and where $\bar{r}_I^P := r_I^P / r_I^P$ is the unit direction along r_I^P. The bars on $\bar{\bar{F}}(r)$ indicate that the force function $F(r)$ is modified by the mapping $\bar{\Omega}_J(\boldsymbol{x}_I) \to \boldsymbol{x}_I^P$. Depending on the problem, the reduction of

RESEARCH ARTICLE

the interaction region $\bar{\Omega}_J(x_I)$ to a surface, or even a point, can lead to a huge gain in efficiency without losing much accuracy, as is demonstrated in the numerical example of Section 2.4. It is emphasized that in the formulations 'SI' and 'PI' the volume $\bar{\Omega}_J(\boldsymbol{x}_I)$ is not neglected, but captured through the mapping procedure. In (Ref. [1]) this mapping is accomplished by approximate analytical integration.

Figure 2 and the discussion above introduce one level of approximation, namely the reduction of the influencing region $\bar{\Omega}_J(x_I)$. A second level of approximation is the reduction of domain $\bar{\Omega}_I$, the region where body forces $\mathbf{b}_I$ are invoked. This second level, which we use in our particular implementations of formulations 'SI' and 'PI',[1] is to project all the body forces $\mathbf{b}_I$ invoked within $\bar{\Omega}_I$ onto the outer surface $\partial\bar{\Omega}_I$. Hence, expression $(25)_1$ is reduced to

$$\delta\Pi_{\mathrm{C},I} = -\int_{\partial\bar{\Omega}_I} \delta\varphi_I \cdot \beta_I t_I \mathrm{d}a_I \tag{28}$$

As indicated, the body force $\mathbf{b}_I$ of Eq. $(25)_1$ is thus reduced to the surface traction $\mathbf{t}_I$. Since the volume integration over $\bar{\Omega}_I$ is reduced to a surface integration over $\partial\bar{\Omega}_I$ a further increase in efficiency is achieved.

The three methods discussed above, apply to arbitrarily shaped bodies Ω_I and Ω_J. Possible implementations of formulations 'VI', 'SI' and 'PI' are discussed in.[42,1] A similar surface formulation, for the case of infinitesimal deformations, has also been derived in.[54,55] We finally note that computational contact approaches for macroscale problems are typically cast in a point formulation, e.g., see Refs. [25], [26]. In this regard, the implementation of method 'PI', proposed in Ref. [1] can be classified as a so called 'Barrier Method.'[30]

2.4. A Simple Comparison

The proposed contact model is motivated as a coarsened description of molecular contact simulations, which, depending on the problem size, can become prohibitively expensive. This section serves the purpose to illustrate the numerical efficiency of the proposed CGC model compared to molecular statics. Therefore a simple contact example is chosen: We consider the case of a cylinder with radius R_0, located between two half-spaces, as is shown in Figure 3(a). The two half-spaces are compressed by the displacement $2u$, with required compressive force P. The motion of the system is considered as quasi-static and in a state of plane strain.

The interaction between cylinder and half-space is governed by the *intersolid* potential ϕ (11), which is characterized by the material parameters r_0 and ϵ_0. A cutoff radius r_c is introduced beyond which the force $F = -\partial\phi/\partial r$ is neglected. Here we chose to neglect forces smaller than $1/100$ of the maximum attraction (which occurs at $r = \sqrt[6]{13/7}r_0$). This yields $r_c \approx 2.39r_0$.

The interaction of the atoms within each body is characterized by the *intrasolid* potential ψ. As an example for the internal structure of the bodies, we consider a face-centered-cubic (fcc) crystal aligned as shown in frame (a). For the present comparison, the intrasolid potential ψ is modelled by nearest neighbor, Lennard-Jones-type interaction, described by

$$\psi(r) = \epsilon_\psi\left(\frac{r_\psi}{r}\right)^{12} - 2\epsilon_\psi\left(\frac{r_\psi}{r}\right)^{6} \tag{29}$$

Here r_ψ is the equilibrium spacing of the undeformed crystal lattice, and ϵ_ψ is the energy characterizing the intrasolid atomic bond. This simple model for the internal structure is chosen since the emphasis of the present work is placed on the study of the intersolid interaction modelled by Π_{C} (12), rather than the study of the intrasolid interaction modelled by Π_{int} (8).

In the undeformed configuration the atomic density is obtained as $\beta_0 = \sqrt{2}/r_\psi^3$. In relation to the cylinder radius R_0 we chose $r_\psi = \sqrt{2}R_0/20$. Thus, if the equilibrium spacing r_ψ is of the order of 0.3 nm, the cylinder radius R_0 measures about 5 nm. The intersolid bond is typically much weaker but of greater range than the intrasolid bond. We therefore chose $r_0 = 2r_\psi$ and $\epsilon_\psi = 4000\ \epsilon_0$. The system is normalized by the length parameter R_0 and the energy density $W_0 := \beta_0\epsilon_\psi$.

The atomic lattice and a finite element mesh chosen for this example are shown in Figure 3(c). They are displayed next to each other for comparison (they are separate models with is no coupling considered in between). The atomic lattice contains 2022 atoms corresponding to 4044 degrees of freedom (dofs), whereas the FE mesh contains only 57 elements and 154 dofs. The atoms shaded dark are located the distance $r_\psi/\sqrt{2}$ below the grey shaded atoms. The discrete model is simulated using Eqs. (7) and (10). The continuum CGC model is simulated using a finite element formulation of Eqs. (8) and (12). In the latter case the Cauchy-Born rule is used to evaluate (9). Frame (d) shows the deformation of lattice and FE mesh (using method 'SI') for an imposed displacement $u = 0.5\ R_0$. The general agreement between the two solutions (relative to the global parameter R_0) is very close. This is further illustrated in frame (e), which shows a superimposition of the two configurations. It can be seen that the detailed atomic surface displacements (relative the local parameter r_ψ) cannot be captured exactly by the finite element solution. These detailed surface displacements are strongly influenced by the atomic placement, as is noted in Ref. [56]. For the two solutions shown in frame (e), the deformation farther away from the zone of contact matches nicely. In particular, the deformation in the lower right corner of frame (e) confirms the affine motion of the lattice according to the Cauchy-Born rule. Frame (e) also displays the stress $I_1 = \mathrm{tr}\sigma$ from the finite element computation. A comparison of the load-displacement curves of the three CGCM formulations, discussed in Section 2.3, and the molecular computation is displayed in frame (b).

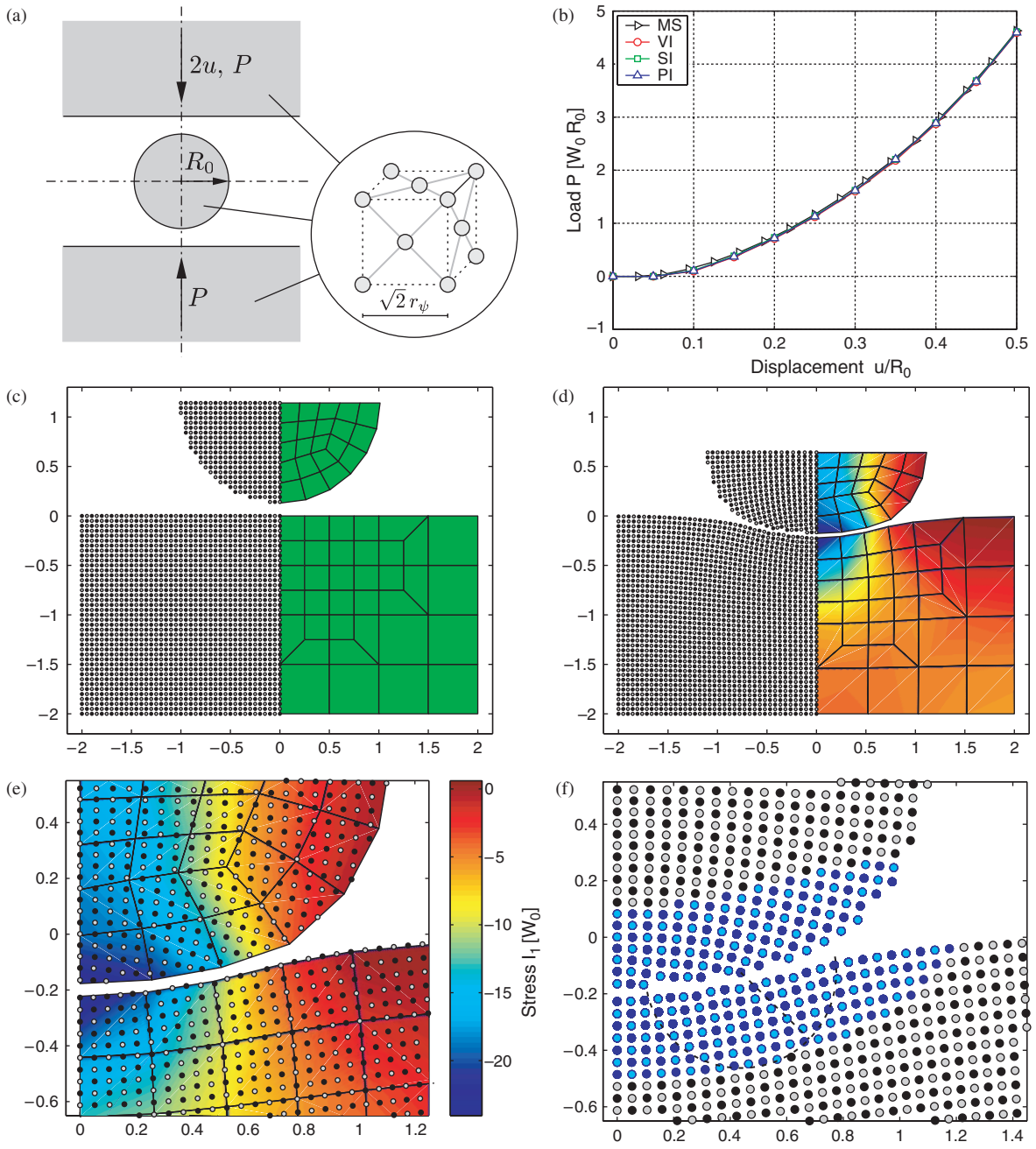

Fig. 3. Comparison of molecular statics (MS) and the CGC model: (a) Model problem; (b) Load-displacement curve; (c) Undeformed and (d) deformed atomic lattice and FE mesh; (e) Superimposed deformation; (f) Regions of intersolid interaction.

Again, the overall agreement (relative to R_0) between the four simulations is very good. Frame (f) shows the regions of intersolid interaction between the two bodies. As illustrated in Section 2.3, these zones denote the regions contributing to the contact interaction. All atoms colored in light and dark blue in Frame (e) mark the particles which are influenced by the neighboring body, since there is at least one atom from the neighboring body within the distance $r_c = 2.39r_0 = 0.338R_0$. As an example the atom marked in red is influenced by the particles within the shown hemisphere $r \leq r_c$. Including interaction with out-of-plane atoms, this hemisphere contains 315 atoms.

The most important aspect of the above comparison is the efficiency gained by the CGC model. This is displayed in Table I. Here, the total number of intrasolid and intersolid interaction evaluations, needed to solve the problem numerically, are listed. The number of intrasolid interaction evaluations depends on the number of degrees of freedom (dofs). As the number of dofs reduces from the molecular model to the finite element model, fewer intrasolid evaluations are counted. The number of required

RESEARCH ARTICLE

Table I. Computational efficiency of the coarse-grained contact model.

	MS	VI	SI	PI
Number of atoms / finite elements	2022	57	57	57
Number of intrasolid interaction evaluations	24264	1368	1368	1368
Number of intersolid interaction evaluations	7387	4832	270	46
CPU time	203 s	1.39 s	0.34 s	0.31 s

intrasolid evaluations determines the computational time to set up the virtual work $\delta\Pi_{\text{int}}$. The number of intersolid evaluations determines the computational time to set up the virtual work $\delta\Pi_{\text{C}}$. Due to the reduced integration discussed in Eqs. (25)–(28) the formulations 'VI', 'SI' and 'PI' are increasingly more efficient than the MD model. For the determination of the values listed in Table I see Ref. [42]. Because of the significant decrease in intersolid and intrasolid interaction evaluations between the various methods, we observe a substantial decrease in the CPU time (measured on an Intel P4 3.0 GHz CPU). In summary it can be seen that there is an increase in speed when going from molecular statics to formulations 'VI', 'SI' and 'PI' due to the decrease in the number of dofs and in the number of intersolid interactions to evaluate. The computational cost to obtain $\delta\Pi_{\text{int}}$ and $\delta\Pi_{\text{C}}$ scales linearly with the number of intrasolid and intersolid interaction evaluations. The solution time to solve the resulting equilibrium equations is controlled by the number of dofs. As the problem size increases the savings can become even more dramatic.

It is emphasized that the comparison of the above example is by no means exhaustive, as it is restricted to reversible (i.e., elastic), quasi-static and temperature independent conditions. Also, more complicated intrasolid potentials can be used for a more realistic description of the internal bonding. It is further noted that the savings in efficiency are inevitably linked to a loss of information. For instance, the coarse finite element description of the problem shown in Figure 3 will not be able to accurately capture details at the atomic scale. More detailed studies of mechanical contact can be found in the literature, for example considering dislocations,[57,58] grain boundaries,[23] surface roughness,[22] or phase transformation and electrical resistance.[24] We emphasize that the objective of this research is not such detailed modelling, but rather the development of a homogenized or coarse-grained contact formulation and its efficient implementation. We seek a model that can be employed over a wide range of length scales as is illustrated in the following section.

3. SCALING OF THE COARSE-GRAINED CONTACT MODEL

In the preceding section we have outlined and derived a nanoscale continuum contact model based on the coarse-graining of molecular dynamics. The model, termed the Coarse-Grained Contact Model, depends on several parameters. In the following we focus on the scaling[59] of the CGC model with respect to these parameters. A scaling investigation is important for the understanding on how the output of a given model is affected by the input parameters, i.e., we wish to know how the model behavior changes if the model parameters are varied. Conversely, we want to understand how the model parameters should change in order to obtain different model behavior. Scaling is further important to identify similarities in the model behavior for different input parameters. Such similarities then allow the experimental investigation of the model behavior for inaccessible parameters by using accessible ones.

In the following discussion we consider the case of contact between a sphere, with radius R_0, and an half-space, as shown in Figure 4(a). The considered problem is quasi-static. The internal response of the contacting bodies is modelled by an isotropic Neo-Hookean material model defined by the strain energy density (per reference volume)

$$W = U(J) + \frac{\mu}{2}(I_1 - 3) - \mu \ln J \quad U(J) = \frac{\Lambda}{2}(\ln J)^2 \quad (30)$$

with the parameters $\mu = E_Y/2/(1+\nu)$ and $\Lambda = 2\mu\nu/(1-2\nu)$, where E_Y and ν correspond to Young's modulus and Poisson's ratio. All three bodies are supposed

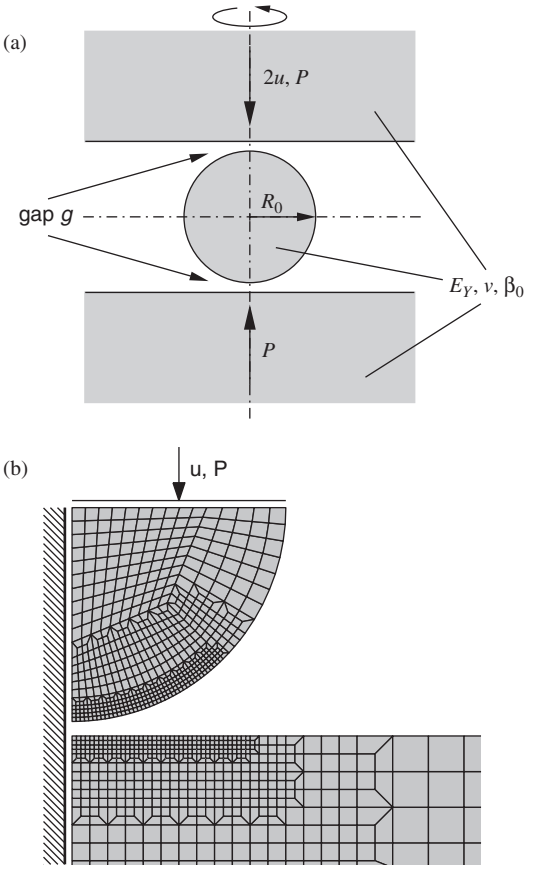

Fig. 4. Spherical contact: (a) Model problem; (b) Finite element mesh.

RESEARCH ARTICLE

to have the same material constants E_Y and ν. Such a simplified constitutive model is useful, since we are mainly interested in the scaling of the contact interaction as modelled by contribution Π_C (12). For the given problem, the model parameters are

- the prescribed displacement u,
- the geometry parameter R_0,
- the material constants E_Y, ν and β_0, and
- r_0 and ϵ_0, the parameters of the intersolid interaction potential ϕ (11).

In general, the mechanical behavior B of the considered model problem depends on these seven parameters, i.e.,

$$B = f(u, R_0, E_Y, r_0, \epsilon_0, \beta_0, \nu) \tag{31}$$

We further simplify the model by considering a fixed material structure such that the reference density β_0 is related to r_0 by $\beta_0 = c_0/r_0^3$ for some constant c_0. For now, also ν is considered fixed (at $\nu = 0.2$), so that E_Y is the only variable in the material response. The behavior B is thus given by

$$B = f(u, R_0, E_Y, r_0, \epsilon_0) \tag{32}$$

Obviously, the functions f in Eqs. (31) and (32) are different. Here, u, R_0 and r_0 are length scales, whereas ϵ_0 has units of energy and E_Y has units of energy density. Let us introduce the energy densities $W_0 := E_Y$ and $w_0 := c_0\beta_0\epsilon_0$ $(= r_0^3\beta_0^2\epsilon_0)$ to write

$$B = f(u, R_0, W_0, r_0, w_0) \tag{33}$$

i.e., the mechanical behavior is a function of the length scales u, R_0, r_0 and the energy densities W_0, w_0. The behavior B itself must have combined units. According to the Π-Theorem[59] relation (33) can be normalized and thus reduced by one length parameter and one energy density parameter. We can thus write

$$\bar{B} = f(\bar{u}, \gamma_L, \gamma_W) \tag{34}$$

where

$$\gamma_L := \frac{R_0}{r_0} \quad \gamma_W := \frac{W_0}{w_0} \tag{35}$$

By $\bar{B}$ and $\bar{u}$ we denote the normalization of B and u. In the following we consider the behavior of the gap g, see Figure 4(a), the behavior of the load P and the behavior of the Cauchy stress $\boldsymbol{\sigma}$, that is, we consider the three cases $B = g$, $B = P$ and $B = \boldsymbol{\sigma}$. Together with u they can either be normalized as

$$\bar{g} = \frac{g}{R_0}, \quad \bar{P} = \frac{P}{W_0 R_0^2}, \quad \bar{\boldsymbol{\sigma}} = \frac{\boldsymbol{\sigma}}{W_0}, \quad \bar{u} = \frac{u}{R_0} \tag{36}$$

or, alternatively, as

$$\bar{g} = \frac{g}{r_0}, \quad \bar{P} = \frac{P}{w_0 r_0^2}, \quad \bar{\boldsymbol{\sigma}} = \frac{\boldsymbol{\sigma}}{w_0}, \quad \bar{u} = \frac{u}{r_0} \tag{37}$$

i.e. either by the global parameters R_0 and W_0, or by the local parameters r_0 and w_0. In the remainder of this section we consider normalization (37). The examples of Section 2.4 and 4 are normalized by scheme (36). By establishing expression (34), we have formally shown that the behavior of the considered model problem, e.g. the gap g, the load P and the stress field $\boldsymbol{\sigma}$, depends only on the prescribed displacement $\bar{u}$ and the two model parameters γ_L and γ_W. Parameter γ_L $(35)_1$, the ratio between cylinder radius R_0 and intersolid equilibrium spacing r_0, is a geometrical quantity characterizing the size of the considered problem. Parameter γ_W $(35)_2$, the ratio between the energy densities $W_0 = E_Y$ and $w_0 = c_0\beta_0\epsilon_0$, characterizes the strength of the intrasolid bond ψ versus the strength of the intersolid bond ϕ. If γ_W increases the intrasolid bond increases in strength compared to the intersolid bond.

Some aspects of the dependence of the load P and the gap g on $\bar{u}$, γ_L and γ_W, according to relation (34), have been examined in.[30] In this paper we further show that, by introducing the combined parameter

$$\gamma_c := \gamma_W^2/\gamma_L \tag{38}$$

certain aspects of the behavior B are described by the significantly simpler relation

$$\bar{\bar{B}} = f(\bar{u}, \gamma_c) \tag{39}$$

i.e., B is characterized by only two variables. Here $\bar{\bar{B}}$ denotes a different normalization from $\bar{B}$. Relation (39) applies to a certain extend to the load P, the gap g and the stress field $\boldsymbol{\sigma}$. As is shown below, some aspects of P and $\boldsymbol{\sigma}$ do not follow (39) and are thus no further simplified than by relation (34). A formal derivation of (39), based on dimensional analysis, like the derivation of (34), is not possible. Such problems are characterized by 'incomplete similarity'.[59]

To demonstrate the validity of Eq. (39) we consider the 14 cases for $\gamma_L \in \{5, 10, 20, 50, 100, 200, 500\}$ combined with $\gamma_c = 70$ and $\gamma_c = 7000$. Since r_0 is typically on the order of nanometers, the given list of values for γ_L corresponds to problem sizes ranging from nanometers to micrometers. The load displacement curve $P(u)$ and the gap $g(u)$ for the 14 considered cases are displayed in Figure 5. These and the following results of this section are obtained by a finite element analysis using the mesh shown in Figure 4(b) and considering the point formulation derived in.[1] To satisfy relation (39), the load must be normalized as $\bar{\bar{P}} = P/(w_0 r_0^2 \gamma_L)$. The gap satisfies (39) for $\bar{\bar{g}} = g/r_0$, i.e. by the normalization according to Eq. (37).

Before analyzing the influence of parameter γ_c, let us discuss the behavior of P and g in dependence of the prescribed displacement u. The contact behavior, which reflects the behavior of the Lennard-Jones potential (11), can be characterized by three phases, denoted as Phase I, II and III in Figure 5. At first, two bodies, initially far apart,

RESEARCH ARTICLE

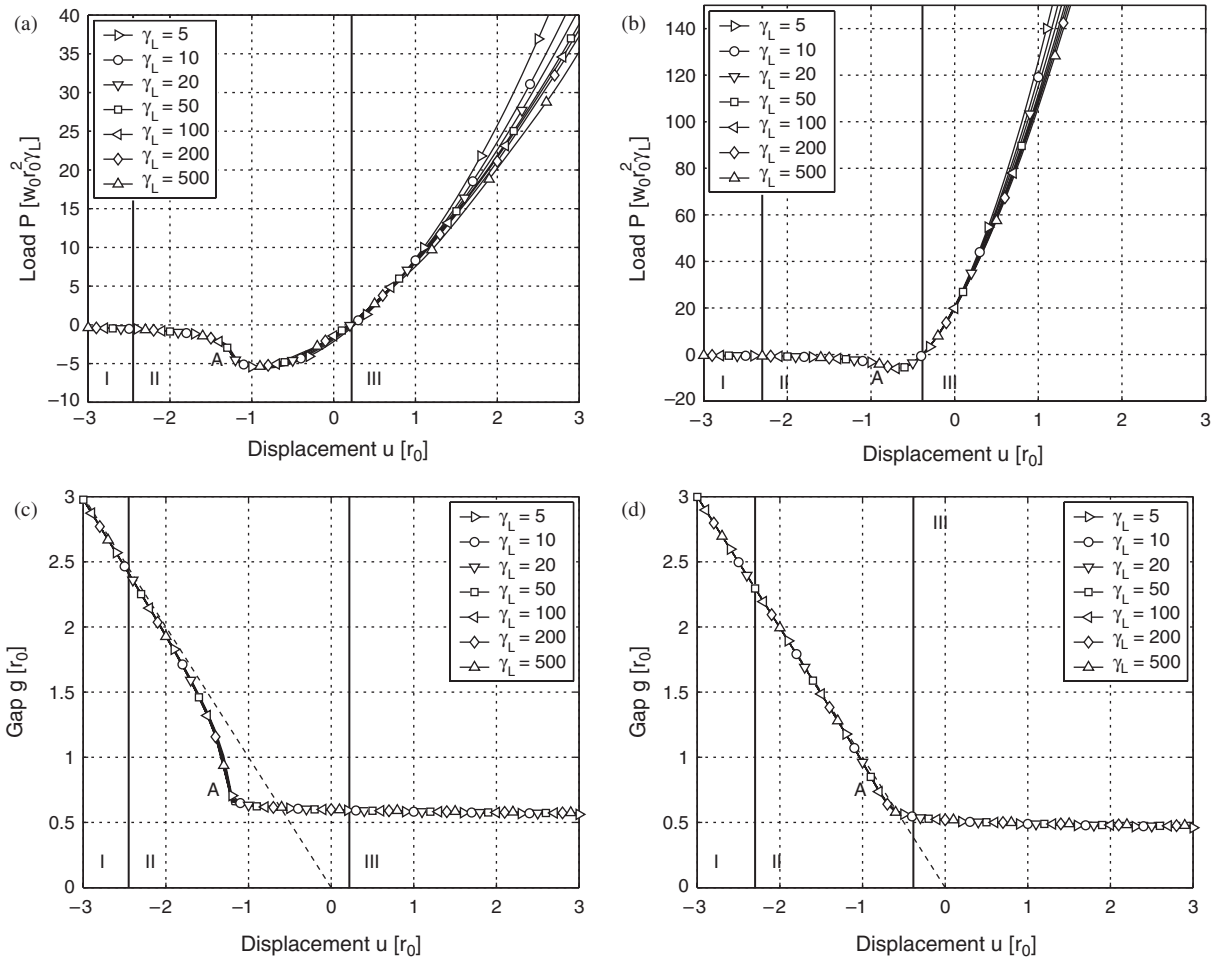

Fig. 5. Load-displacement curve $P(u)$ for (a) $\gamma_c = 70$ and (b) $\gamma_c = 7000$; Gap $g(u)$ for (c) $\gamma_c = 70$ and (d) $\gamma_c = 7000$.

approach each other without yet interacting, i.e. $P \approx 0$. Their motion is rigid and we therefore term this phase as the *rigid phase* (Phase I). As the bodies come closer, an attractive or adhesive force, $P < 0$, appears and we therefore denote this phase as the *adhesion phase* (Phase II). The adhesion takes a maximum at $P_{\min}$. It can be seen from the results of Frames (a) and (b), that $P_{\min}/W_0 R_0^2$ decreases linearly with γ_L and γ_W (since $P_{\min}/(w_0 r_0^2 \gamma_L) = P_{\min}\gamma_L\gamma_W/(W_0 R_0^2)$ is approximately constant). As the two bodies are further pushed together, the force changes sign and becomes compressive ($P > 0$). We denote the phase where $P > 0$ the *contact phase* (Phase III). It can be seen that for large compressive forces $P \gg 0$ the seven curves displayed in Frame (a) and (b) diverge, which implies that relation (39) looses its applicability. The reason for this behavior probably lies in the nonlinear deformation of the solids. In case of $g(u)$, displayed in Frames (c) and (d), the scaling relation (39) remains valid throughout all phases. The displacement $u = 0$ is calibrated from the intersection of the dashed line, displayed in Frames (c) and (d), with $g = 0$. This dashed line indicates the behavior of $g(u)$ if the sphere and half-space were to approach each other without interacting. The intersection of the dashed line with $g = 0$ then corresponds to the hypothetical case where the two bodies are touching each other. During phase I, the gap g decreases linearly with u, whereas, during phase III, the gap hardly changes with u. In Phase III the displacement u is accommodated by the deformation of the solids. Let us define the contact gap g_c as the gap for a fixed u in Region III. From Frames (c) and (d) it can be observed that g_c/r_0 is constant with γ_L; therefore g_c/R_0 decreases linearly with γ_L. It is noted that the boundary between Phases I and II is not a rigorous boundary. It marks the point beyond which P may be neglected. In the figure we chose $P = P_{\min}/10$ as the threshold value.

Now, let us discuss the dependence of P and g on parameter γ_c. Comparing Frames (a) and (b) we observe that the slope P' during the contact Phase (III) decreases along with γ_c. It can be further seen that the adhesion Phase (II) shrinks with increasing γ_c, and that during Phase II the downward slope of P and g at point A steepens as γ_c decreases. In fact, below a threshold value of γ_c, the behavior of $P(u)$ turns unstable at point A. This unstable behavior leads to the effects known

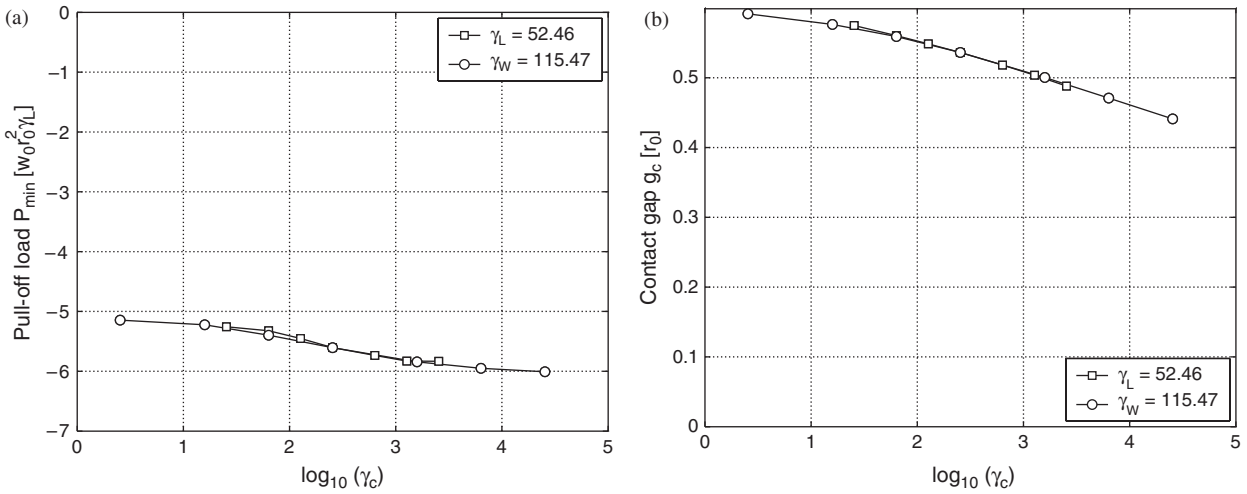

Fig. 6. Pull-off force $P_{\min}$ and contact gap g_c in dependence of parameter $\gamma_c = \gamma_W^2/\gamma_L$ for $\gamma_L = 50\sqrt[6]{4/3}$ and $\gamma_W = 200/\sqrt{3}$.

as 'jump-to-contact' and 'jump-off-contact'.[3] Figure 6 shows the behavior of the minimum force $P_{\min}$ and the contact gap g_c (measured at $u = r_0$) in dependence of parameter γ_c. It is seen that the absolute value of $P_{\min}$ increases with γ_c, while g_c decreases with γ_c. The force $P_{\min}$ is also known as the maximum pull-off load, since it corresponds to the force required to separate the adhering bodies. The results displayed in Figure 6 are taken from two computational series, one with fixed γ_L and one with fixed γ_W, which have also been considered in Ref. [30]. As $\gamma_W \to \infty$ for fixed γ_L (i.e., $\gamma_c \to \infty$), the interaction forces between the two bodies vanish and therefore $g_c \to 0$.

Next, we study the size effect on the deformation and stress field $\boldsymbol{\sigma}$ within the two contacting bodies. We consider the cases $\gamma_L \in \{5, 10, 20, 50, 100, 200\}$ for the fixed displacement $u = -0.5 r_0$ and for fixed $\gamma_c = 70$. Figure 7 shows the deformed configurations and vertical stress component $\boldsymbol{\sigma}_y$ for these six cases. It is seen that the magnitude and the general distribution of $\boldsymbol{\sigma}_y$ obey scaling law (39). The deformation of the two bodies, on the other hand,

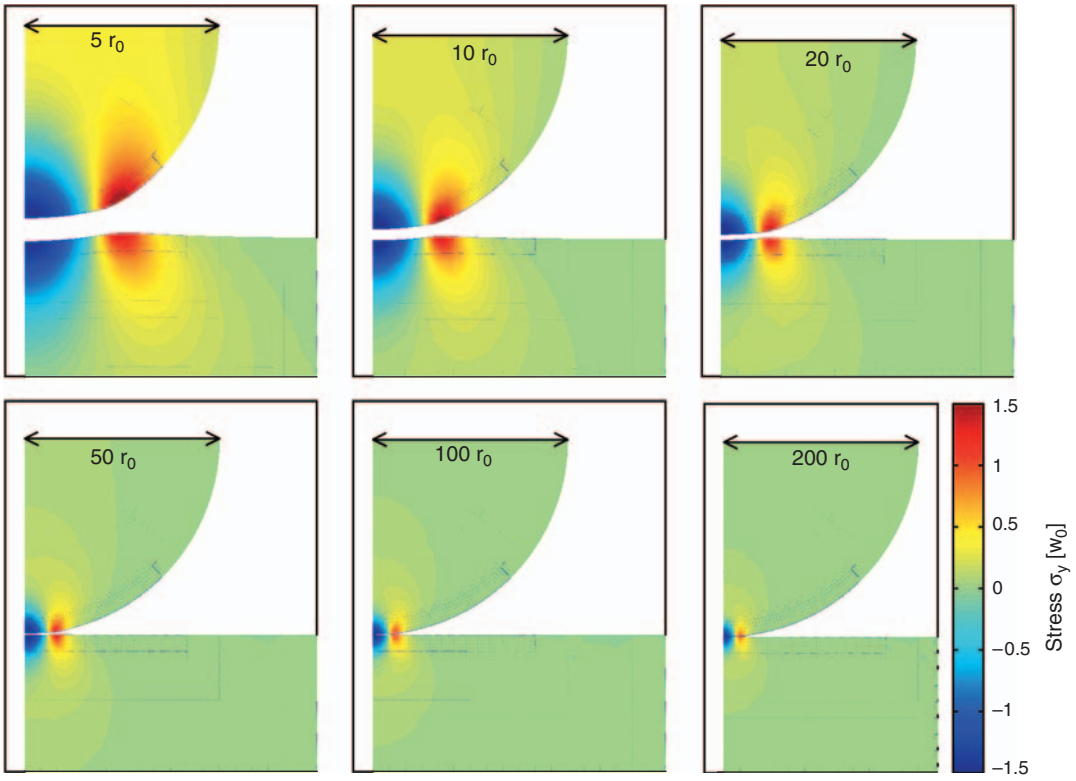

Fig. 7. Deformation and stress $\boldsymbol{\sigma}_y$ at $u = -0.5\ r_0$ for $\gamma_c = 70$ and $\gamma_L \in \{5, 10, 20, 50, 100, 200\}$.

depends explicitly on γ_L, i.e., the deformation obeys relation (34) and not (39). As is shown in Figure 7, compressive stresses (colored blue) develop along the center axis, due to the repulsion of the two bodies during contact. At the fringe of the contact zone, where the gap between the two bodies increases, tensile stresses (shown in red) appear, due to the strong adhesion between the interacting bodies. It is seen that for changing γ_L, the repulsive and attractive stress zones shift towards the center axis and thus different regions of the sphere and half-space are affected. It is recalled that for the six cases in Figure 7, the load $P/(w_0 r_0^2 \gamma_L)$ is constant, as noted in Figure 5(a). The development displayed in Figure 7 shows that as γ_L increases, it becomes more and more difficult to resolve the stresses and deformation with the finite element mesh given in Figure 4(b). A related problem is that the contact interaction force $F = -(\partial\phi/\partial r)$, given through the intersolid potential (11), becomes increasingly difficult to resolve with the given mesh for increasing γ_L. We must therefore either refine the finite element mesh, hence losing efficiency, or risk numerical ill-conditioning. In (Ref. [42]) a modification to the CGCM is proposed, based on a second level of coarse-graining, that maintains efficiency without becoming ill-conditioned. The model can then be applied to even larger scales.

Concluding Section 4 we note that scaling law (34) not only applies to the discussed benchmark problem, but also applies to all other problems that can be formalized by the discussion leading to Eq. (34). In this regard the discussion of this section is twofold, as it illustrates the scaling of a model—the CGC model—by using a simple contact example, while also illustrating the scaling of a problem—spherical contact—by using a novel model.

4. SLIDING EXAMPLE

As an application of the CGC model we consider the sliding contact of two parabola-shaped bodies as is shown in Figure 8(b). Such an idealized contact mechanism can occur between the surface asperities of two sliding, rough bodies, as is indicated by frame (a). The two surface asperities are modelled by the elastic, Neo-Hookean constitutive model (30). The stiffness of the lower asperity is given by E_Y. The upper asperity is modelled twice as stiff, by $2E_Y$. Both asperities have Poisson's ratio $\nu = 0.3$. The problem is considered as a plane strain problem with the chosen parameters $\gamma_L = 20$ and $\gamma_W = 50$ (with $W_0 = E_Y$) according to Eq. (35). The asperities are analyzed with the finite element method using the mesh shown in frame (b). The point-formulation ('PI'), as developed in,[1] is used to integrate $\delta\Pi_{C,I}$ according to Eq. (28).

Figures 9(b)–(f) show the deformation and the von Mises stress σ_v (displayed as $\log_{10}(\sigma_v/W_0)$) within the two asperities. As can be expected the largest stress and deformation develops in the softer, lower asperity. The lower body is pushed at its base by an imposed displacement u. The resultant horizontal reaction at this boundary, P, as a function of u is shown in frame (a). The open circles correspond to the five configurations shown in frames (b)–(f). The initial hump at point A indicates that strong adhesion occurs prior to contact. As has been discussed along with Figure 5, adhesion is a long-range effect, which characterizes the attractive behavior for larger separations. During contact, attractive forces are present at the fringe of the contact zone, but they are overpowered by the repulsive forces at the center. The two asperities are undeformed and stress free at the beginning and the end of the sliding process. The work required to move the asperities is given by the area under $P(u)$. It can be confirmed numerically that the total work for this process is identical to zero, i.e. the considered process, and thus the contact formulation 'PI', is energy conserving and frictionless. This property of formulation 'PI' follows from its construction discussed in Section 2.3. According to Figure 2(c), the interaction forces $\mathbf{b}_I$ for formulation 'PI' are normal to $\partial\Omega_J$ and are hence frictionless. If dissipative processes are considered, e.g., through an inelastic material response, the total energy of this sliding example is not conserved. Such dissipative processes at the microscale would be perceived as friction on the macroscale. Through dissipative interaction of surface asperities, one may thus model global sliding friction, even when no sliding friction occurs locally.

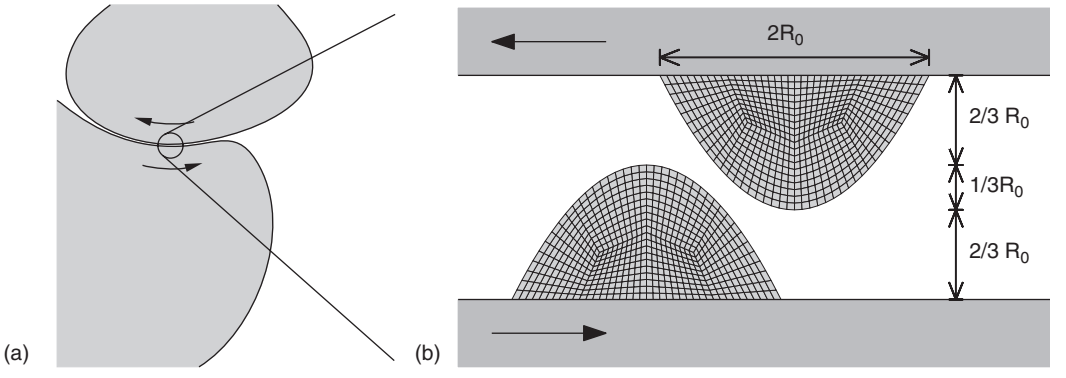

Fig. 8. Sliding contact: (a) Macroscopic sliding; (b) Microscopic view of interface asperities and chosen finite element mesh.

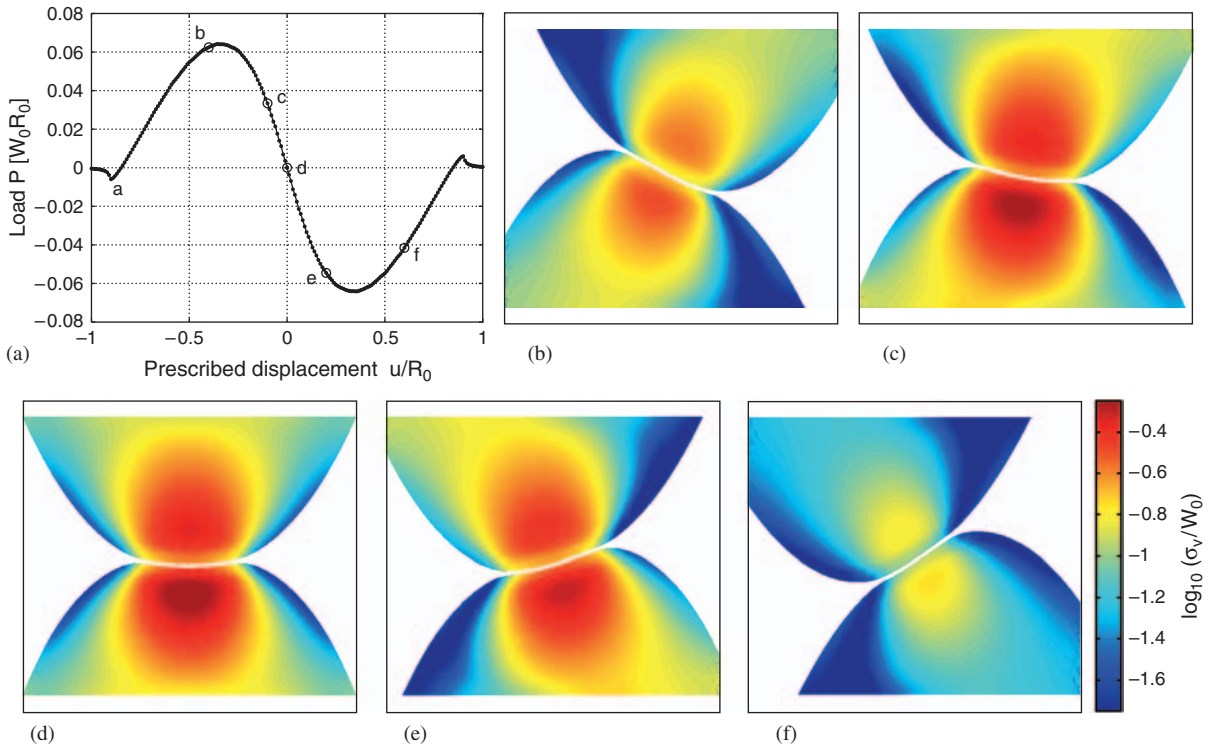

Fig. 9. (a) Load-displacement curve; (b)–(f) Deformation and von Mises stress σ_v of the two contacting asperities at the states shown as open circles in frame (a).

Since the CGC model is a homogenized description of interatomic contact, it cannot capture all the detailed effects occurring at the atomic level. One such phenomenon, discussed in,[60] is that even atomically flat surfaces can offer weak resistance against sliding motion. Another effect, that can occur during sliding, is the abrasion of surface particles. This abrasion changes the surface topology and thus affects the sliding motion and sliding force $P(u)$. As a refinement of the proposed contact description, both these effects may be homogenized and included into the framework of the CGCM.

5. CONCLUSION

In this work we have presented the theory, scaling and applicability of a nanoscale contact model, termed the Coarse Grained Contact Model. As is shown in Section 2.1, the model is a combination of particle oriented and continuum oriented contact modelling. In this sense the model can be viewed both as the refinement of continuum contact mechanics or as the coarsening of a molecular dynamics contact model. In Sections 2.2 and 2.3, the governing weak form of the CGC model (24) is derived and efficient formulations for the evaluation of the virtual contact work $\delta\Pi_C$ are discussed. A comparison between molecular statics and the CGC model is given in Section 2.4, which validates and illustrates the accuracy and efficiency of the proposed contact-interaction model. In Section 3 the scaling of the CGC model is investigated in detail. Using a benchmark model problem, it is shown that the behavior of the CGC model follows the scaling law (34) and that several model aspects even follow relation (39). To illustrate an application of the proposed contact model, Section 4 shows the contact interaction of two surface asperities.

The formulation of the proposed model allows the investigation of interaction, like adhesion and contact, between arbitrarily shaped nanoscale continua under large deformations. The model can be used to describe the interaction between carbon nanotubes,[1] model adhesive contact of spheres and study interfacial sliding mechanisms, as is shown in Sections 3 and 4. For the case of spherical contact, we have shown in[30] that in the small deformation regime the results of the CGC model are in excellent agreement with the analytical Maugis-Dugdale[33] model, which contains the JKR[31] and DMT[32] models as special cases. The formulation of the CGC model admits the use of any two-point potential ϕ to describe the intersolid interaction. Examples other than van der Waals interaction include electrostatic Coulomb interaction between charged particles. As is shown in,[1] the CGC model can be applied to the interaction of multiple bodies. As has been mentioned in Section 3, the present formulation becomes either inefficient or ill-conditioned as the problem size increases in scale, i.e., as parameter γ_L becomes too big. This problem can be avoided by introducing a second level of coarse-graining as is proposed in Ref. [42].

By the scaling study of Section 3 we have shown how the model parameters affect the behavior of the CGC model. Using a simple model problem and dimensional analysis, the initial set of model parameters is substantially reduced. The remaining important parameters are γ_L and γ_W, which describe the problem size and the strength of adhesion.

Due to its flexibility, the CGC model provides a suitable computational tool for the study of a variety of engineering applications, especially those where the intersolid interaction leads to large deformations. This is the case for soft materials or structures such as are found in many biomechanical applications, like the adhesion of individual cells[10] and the adhesion used by the Gecko.[12] This latter example is particularly interesting due to the hierarchical mechanical structure found on the gecko's toes[13] and its inspiration for synthetic adhesives.[61] Other interesting examples are the modelling of sintering, i.e., the bonding of contacting solids, the further investigation of friction, e.g., due to the interaction of asperities as is shown above, and the study of tribology at small scales.[5] Also interesting is the extension of the scaling study to other benchmark problems containing further parameters, e.g., by considering other contact geometries, other constitutive relations and other interaction types.

Acknowledgment: This work is supported by a NSF grant (Grant No. CMS-0239130), which is greatly appreciated.

RESEARCH ARTICLE

References and Notes

1. R. A. Sauer and S. Li, *Int. J. Numer. Meth. Engrg.* **(2007)**.
2. G. Binnig, C. F. Quate, and C. Gerber, *Phys. Rev. Lett.* 56, 930 **(1986)**.
3. B. Cappella and G. Dietler, *Surf. Sci. Reports* 34, 1 **(1999)**.
4. A. C. Fischer-Cripps, *Nanoindentation*, 2nd edn., Springer Verlag, New York **(2004)**.
5. B. Bhushan, (ed.), *Nanotribology and Nanomechanics*, Springer, New York **(2005)**.
6. R. S. Ruoff, J. Tersoff, D. C. Lorents, S. Subramoney, and B. Chan, *Nature* 364, 514 **(1993)**.
7. T. Hertel, R. Martel, and P. Avouris, *J. Phys. Chem. B* 102, 910 **(1998)**.
8. D. Qian, W. K. Liu, S. Subramoney, and R. S. Ruoff, *J. Nanosci. Nanotech.* 3, 185 **(2003)**.
9. B. H. Thornton and D. B. Bogy, *IEEE Trans. Magn.* 39, 2420 **(2003)**.
10. Y.-S. Chu, S. Dufour, J. P. Thiery, E. Perez, and F. Pincer, *Phys. Rev. Lett.* 94, 028102 **(2005)**.
11. K. Autumn, Y. A. Liang, S. T. Hsieh, W. Zesch, W. P. Chan, T. W. Kenny, R. Fearing, and R. J. Full, *Nature* 405, 681 **(2000)**.
12. K. Autumn, M. Sitti, Y. A. Liang, A. M. Peattie, W. R. Hansen, S. Sponberg, T. W. Kenny, R. Fearing, J. N. Israelachvili, and R. J. Full, *Proc. Natl. Acad. Sci. USA* 99, 12252 **(2002)**.
13. H. Gao, X. Wang, H. Yao, S. Gorb, and E. Arzt, *Mech. Mater.* 37, 275 **(2005)**.
14. T. Hertel, R. E. Walkup, and P. Avouris, *Phys. Rev. B* 58, 13870 **(1998)**.
15. T. Schlick, *Molecular Modelling and Simulation: An interdisciplinary Guide*, Springer, New York **(2002)**.
16. J. Li, A. H. W. Ngan, and P. Gumbsch, *Acta Mater.* 51, 5711 **(2003)**.
17. E. B. Tadmor, M. Ortiz, and R. Phillips, *Phil. Mag. A* 73, 1529 **(1996)**.
18. R. E. Miller and E. B. Tadmor, *J. Comp. -Aid. Mat. Design* 9, 203 **(2002)**.
19. R. E. Rudd and J. Q. Broughton, *Phys. Rev. B* 58, R5893 **(1998)**.
20. R. E. Rudd and J. Q. Broughton, *Phys. Rev. B* 72, 144104 **(2005)**.
21. R. A. Iglesias and E. P. M. Leiva, *Acta Mater.* 54, 2655 **(2006)**.
22. B. Luan, S. Hyun, J. F. Molinari, N. Bernstein, and M. O. Robbins, *Phys. Rev. E* 74, 046710 **(2006)**.
23. F. Sansoz and V. Dupont, *Proc. NSTI Nanotech. 2006 Conference* **(2006)**, Vol. 1 pp. 50–53.
24. G. S. Smith, E. B. Tadmor, N. Bernstein, and E. Kaxiras, *Acta Mater.* 49, 4089 **(2001)**.
25. P. Wriggers, Computational Contact Mechanics, Wiley, Chichester **(2002)**.
26. T. A. Laursen, Computational Contact and Impact Mechanics: Fundamentals of Modelling Interfacial Phenomena in Nonlinear Finite Element Analysis, Springer, Berlin **(2002)**.
27. S.-S. Cho and S. Park, *Trib. Int.* 37, 763 **(2004)**.
28. A. Y. Suh, N. Yu, K. M. Lee, A. A. Polycarpou, and H. T. Johnson, *J. Appl. Phys.* 96, 1348 **(2004)**.
29. J.-J. Wu, *J. Phys. D: Appl. Phys.* 39, 351 **(2006)**.
30. R. A. Sauer and S. Li, *Finite Elem. Anal. Des.* 43, 384 **(2007)**.
31. K. L. Johnson, K. Kendall, and A. D. Roberts, *Proc. Roy. Soc. A.* 324, 301 **(1971)**.
32. B. V. Derjaguin, V. M. Muller and Y. P. Toporov, *J. Colloid Interface Sci.* 53, 314 **(1975)**.
33. D. Maugis, *J. Colloid Interface Sci.* 150, 243 **(1992)**.
34. D. Frenkel and B. Smit, Understanding Molecular Simulation: From Algorithms to Applications, 2nd edn., Academic Press, San Diego **(2001)**.
35. J. N. Israelachvili, Intermolecular and Surface Forces, 2nd edn., Academic Press, London **(1991)**.
36. P. Chadwick, Continuum Mechanics - Concise Theory and Problems, Second Dover Edition, Mineola **(1999)**.
37. M. E. Gurtin, An Introduction to Continuum Mechanics, Academic Press, New York **(1981)**.
38. T. Belytschko, W. K. Liu, and B. Moran, Nonlinear Finite Elements for Continua and Structures, Wiley: Chichester **(2000)**.
39. T. J. R. Hughes, The Finite Element Method - Linear Static and Dynamic Finite Element Analysis, Dover, Minola **(2000)**.
40. O. C. Zienkiewicz and R. L. Taylor, The Finite Element Method, Volumes 1–3, 5th edn., Butterworth-Heinemann, Boston **(2000)**.
41. J. L. Ericksen, edited by M. Gurtin, Phase Transformations and Material Instabilities in Solids, Academic Press, New York **(1984)**, pp. 61–77.
42. R. A. Sauer, An Atomic Interaction based Continuum Model for Computational Multiscale Contact Mechanics, Dissertation, University of California, Berkeley **(2006)**.
43. R. A. Gingold and J. J. Monaghan, *Mon. Not. Roy. Astr. Soc.* 181, 375 **(1977)**.
44. J. J. Monaghan, *Annu. Rev. Astron. Astrophys.* 30, 543 **(1992)**.
45. I. Goldhirsch and C. Goldenberg, *Eur. Phys. J. E* 9, 245 **(2002)**.
46. G. Zanzotto, *Acta. Crys.* A52, 839 **(1996)**.
47. M. S. Daw, S. M. Foiles, and M. I. Baskes, *Mater. Sci. Rep.* 9, 251 **(1993)**.
48. H. S. Park, P. A. Klein, and G. J. Wagner, *Int. J. Numer. Meth. Engng.* 68, 1072 **(2006)**.
49. R. Tadmor, *J. Phys. Condens. Matter* 13, L195 **(2001)**.
50. R. S. Bradley, *Phil. Mag.* 13, 853 **(1932)**.
51. H. C. Hamaker, *Physica* 4, 1058 **(1937)**.
52. M. Arroyo and T. Belytschko, *J. Mech. Phys. Solids* 50, 1941 **(2002)**.
53. R. W. Ogden, Non-Linear Elastic Deformations, Dover, Mineola **(1997)**.

54. C. Argento and A. Jagoda, *J. Mech. Phys. Solids* 45, 1161 **(1997)**.
55. A. Jagoda and C. Argento, *J. Colloid Interface Sci.* 191, 326 **(1997)**.
56. B. Luan and M. O. Robbins, *Nature* 435, 929 **(2005)**.
57. E. B. Tadmor, R. Miller, R. Phillips, and M. Ortiz, *J. Mater. Res.* 14, 2233 **(1999)**.
58. T. Zhu, J. Li, K. J. Van Vliet, S. Ogata, S. Yip, and S. Suresh, *J. Mech. Phys. Solids* 52, 691 **(2004)**.
59. G. I. Barenblatt, *Scaling* Cambridge University Press, Cambridge **(2003)**.
60. B. N. J. Persson, *Surf. Sci. Rep.* 33, 83 **(1999)**.
61. M. Sitti and R. S. Fearing, *J. Adhes. Sci. Technol.* 18, 1055 **(2003)**.

Received: 12 January 2007. Revised/Accepted: 23 March 2007.